Journal of Power Sources 239 (2013) 225–233

Contents lists available at SciVerse ScienceDirect

Journal of Power Sources

journal homepage: www.elsevier.com/locate/jpowsour

Graphene/MnO_2-based composites reduced via different chemical agents for supercapacitors

Myeongjin Kim, Yongseon Hwang, Jooheon Kim*

School of Chemical Engineering & Materials Science, Chung-Ang University, Seoul 156-756, Republic of Korea

HIGHLIGHTS

- Nanoneedle MnO_2 is formed on the graphene oxide surface using functional groups.
- GO/MnO_2 composite is reduced to RGO/MnO_2 via chemical reduction by dipping method.
- Both hydrazine hydrate and sodium borohydride are used as reducing agent.
- Hydrazine hydrate is more effective to form electronically conductive channels.
- Enhanced electrical conductivity leads to electrochemical performance.

ARTICLE INFO

Article history:
Received 3 February 2013
Received in revised form
22 March 2013
Accepted 23 March 2013
Available online 5 April 2013

Keywords:
Supercapacitor
Graphene/MnO_2
Nanoneedle
Reducing effect
Electronic conductive channel
Hydrazine hydrate

ABSTRACT

Graphene/MnO_2 composites are synthesized by the chemical reduction of GO/MnO_2 using both hydrazine hydrate (H-RGO/MnO_2) and sodium borohydride (S-RGO/MnO_2) as reducing agents. The morphology and microstructure of the as-prepared composites are characterized by X-ray diffractometry, field-emission scanning electron microscopy, Raman microscopy, thermogravimetric analysis and X-ray photoelectron spectroscopy. Characterizations indicate that MnO_2 is successfully formed on the GO surface and GO is reduced successfully by using both hydrazine hydrate and sodium borohydride as reducing agents. H-RGO/MnO_2 shows higher electrical conductivity than that of S-RGO/MnO_2 since it has a lower concentration of oxygen-containing functional groups. The capacitive properties of the H-RGO/MnO_2 and S-RGO/MnO_2 electrodes are measured using cyclic voltammetry and galvanostatic charge/discharge tests and electrochemical impedance spectroscopy in a three-electrode experimental setup using a 1 M Na_2SO_4 aqueous solution as the electrolyte. The H-RGO/MnO_2 electrode displays a specific capacitance as high as 327.5 F g^{-1} at 10 mV s^{-1}, which is higher than that of the S-RGO/MnO_2 electrode (278.6 F g^{-1}). It is anticipate that the formation of nanoneedle structures of MnO_2 on graphene oxide surfaces after the hydrazine reduction procedure is a promising fabrication method for supercapacitor electrodes.

1. Introduction

Over the past few years, considerable effort has been devoted to the development of alternative energy storage/conversion devices with high power and energy densities due to increased environmental problems and the depletion of fossil fuel resources [1–3]. As charge-storage devices, supercapacitors exhibit high power density, pulse power supply, long cycle life, and highly dynamic charge propagation. Given these traits, supercapacitors have garnered tremendous attention due to the growing demand for power systems that deliver significant energy with high power [4,5].

Numerous materials have been investigated as possible supercapacitor electrodes, including carbonaceous materials, conductive polymers, and transition metal oxides [6,7]. Among these, metal oxide electrode materials have attracted considerable interest due to their large capacitance and fast redox kinetics. Manganese oxide (MnO_2) is generally considered to be the most promising transition metal oxide for the next generation of supercapacitors by virtue of its high energy density, low cost, environmental friendliness, and natural abundance [8,9]. It is well known that the pseudo-capacitive reaction of MnO_2 is a surface reaction, in that only the surface (or a very thin surface layer of the oxide) can participate in the pseudo-capacitive reaction [10]. Therefore, nanometer-thick MnO_2 deposits deliver very high specific capacitances, ranging from 700 to 1380 F g^{-1} [11]. However, micrometer-thick MnO_2 deposits, or deposits in composite electrode forms which contain

* Corresponding author.
E-mail address: jooheonkim@cau.ac.kr (J. Kim).

0378-7753/$ – see front matter © 2013 Elsevier B.V. All rights reserved.
http://dx.doi.org/10.1016/j.jpowsour.2013.03.146

carbon and binders, usually show a low specific capacitance ranging from 150 to 250 F g^{-1}, because of the poor electrical conductivity of MnO_2 and low-accessibility of the surface area [12].

In order to improve the electrochemical performance of MnO_2, intensive studies involving techniques such as nanostructuring, nanocompositing, and mixing of carbon materials have been developed [13–15]. Among these, carbonaceous materials such as activated carbon, carbon aerogels, and carbon nanotubes have been investigated in detail due to their favorable electronic conductivity, high specific area, and high chemical stability [16–18]. Graphene is a newly reported carbon material that has received tremendous attention since Geim succeeded in isolating it from graphite [19]. Over the past few years, there have been several approaches to apply graphene as an electrode material for supercapacitors, considering its large surface area ($\sim$2630 m^2 g^{-1}), excellent electronic conductivity, outstanding chemical stability, and good physical properties [20–27]. Therefore, a hybrid electrode architecture which incorporates nanoscopic MnO_2 on the surface of graphene is thought to be ideal for enhancing electrochemical performance.

There have been many reports of directly deposition of MnO_2 on graphene. Yan et al. suggested hybrid electrode materials through the combination of graphene with MnO_2 [28]. They reduced graphene oxide to graphene by chemical reduction using hydrazine hydrate, after which MnO_2 was formed on the graphene surface. Li et al. synthesized graphene/MnO_2 electrode materials via a similar process, obtaining graphene by thermally expanded graphene oxide [29]. Yan and Li showed maximum specific capacitances of 310 F g^{-1} at a scan rate of 2 mV s^{-1} and 211.5 F g^{-1} at 2 mV s^{-1}, respectively. They obtained enhanced specific capacitance values by exploiting the excellent electronic conductivity of graphene, which can form electronically conductive channels [28]. However, they did not show the nanoneedle structure of MnO_2, which results in an undesirable increase in the surface area and a decrease in the diffusion path.

Some studies have been reported in which MnO_2 was prepared with different morphologies to obtain an enhanced specific capacitance by increasing the specific area of MnO_2. Chen et al. prepared MnO_2 with different crystallographic forms (α, γ) and morphologies (needles, rods, and spindles), and investigated the electrochemical performance. It was reported that the needle-like sample showed higher specific capacitance [30]. Devaraj and Munichandraiah investigated the effect of the crystallographic structure of MnO_2 on its electrochemical capacitance properties, and found that MnO_2 with α and δ crystallographic structures offered higher specific capacitances [31]. Chen et al. suggested electrode materials via the combination of graphene oxide with nanoneedle MnO_2 structures [32]. However, they obtained a relatively lower specific capacitance value (197.2 F g^{-1} at 0.2 A g^{-1}) compared to those obtained by Yan and Li because graphene oxide cannot form electronically conductive channels.

In this study, two types of graphene/MnO_2 composites reduced from GO/MnO_2 using hydrazine hydrate (H-RGO/MnO_2) and sodium borohydride (S-RGO/MnO_2) are prepared. For these composites, the nanoneedle structure of MnO_2 promotes specific area, reversible pseudocapacity, and a decrease in the diffusion path. Graphene nanosheets serve mainly as a highly conductive support, which can also provide a large surface for the deposition of nanoscale MnO_2. The morphology and microstructural characteristics of H-RGO/MnO_2 and S-RGO/MnO_2 were investigated in detail. The electrochemical performance of the two composites prepared (H-RGO/MnO_2 and S-RGO/MnO_2) are also investigated using cyclic voltammetry (CV), galvanostatic charge/discharge experiments, and electrochemical impedance spectroscopy (EIS) and analysis of the specific capacitance and capacitance retention.

2. Experiment

2.1. Synthesis of graphene oxide

Graphene oxide (GO) was synthesized using the modified Hummers method. In a typical synthesis, 3 g of graphite powder was placed into a mixture containing 360 mL of concentrated H_2SO_4 and 40 mL of concentrated H_3PO_4. The resulting mixture was stirred in an ice bath for 4 h. After homogeneous dispersion of the graphite powder in the solution, $KMnO_4$ (18 g) was added slowly over 1 h to the solution in an ice bath at room temperature. The mixture was then stirred for 12 h at 50 °C in an oil bath. After the reaction, the mixture was poured into 400 mL of deionized water (DI) water containing 3 mL of H_2O_2. The mixture was then washed several times and purified with HCl and DI water, respectively. The collected graphite oxide was dispersed in DI water by ultrasonication to exfoliate the graphite oxide into GO, which was dried in a vacuum oven at 80 °C for 2 days.

2.2. Synthesis of graphene/MnO_2 composites

In order to synthesize GO/MnO_2 which are feeding ratio 1/3, GO (0.066 g) and $MnCl_2 \cdot 4H_2O$ (0.27 g) were dispersed in isopropyl alcohol (50 mL), with ultrasonication for 0.5 h. Subsequently, the mixture was heated to approximately 85 °C in a water-cooled condenser with vigorous stirring. Then, $KMnO_4$ (0.15 g) dissolved in 5 mL of DI water was added to the above boiling solution. The obtained mixture was filtered and washed several times, and was finally dried in a vacuum oven at 60 °C for 24 h [32]. Hydrazine hydrate-reduced Graphene/MnO_2 (H-RGO/MnO_2) was obtained by dipping method [33]. The 0.05 g of GO/MnO_2 was dipped in aqueous hydrazine hydrate (20 mM) solution for 24 h. The resulting H-RGO/MnO_2 composites were collected with filtration, washed with DI water several times, and dried in a vacuum oven at 90 °C for 24 h. Also, the sodium borohydride-reduced graphene/MnO_2 (S-RGO/MnO_2) was obtained by a procedure similar to that used to obtain H-RGO/MnO_2, to compare the reducing effect between hydrazine hydrate and sodium borohydride. All of the experimental procedures and conditions were exactly the same; the only difference was that sodium borohydride was used as a reducing agent instead of hydrazine hydrate.

2.3. Characterization methods

XRD patterns were collected by X-ray diffractometer (XRD, New D8-Advance/Bruker-AXS) at a scan rate of 1°s^{-1} with a 2θ range of 5–70° with Cu$K_{\alpha 1}$ radiation (0.154056 nm). Field emission scanning electron microscopy (FE-SEM, SIGMA, Carl Zeiss) was used to examine the morphology of the GO, GO/MnO_2, H-RGO/MnO_2, and S-RGO/MnO_2. Raman spectra were recorded on a Raman Station 400F (Perkin–Elmer), using a near infrared laser operating at 758 nm with a CCD detector. TGA was carried out on a TA instrument TGA-2050 at a heating rate of 10°C min^{-1} in air. XPS analysis was carried out on a VGMicrotech, ESCA2000 system using a spectrometer with an Mg Kα X-ray source (1253.6 eV) and a hemispherical analyzer. During curve fitting, the Gaussian peak widths were constant in each spectrum.

2.4. Supercapacitor preparation and characterization

Fabrication of working electrodes was carried out as follows. The as-prepared materials, carbon black, and poly(vinylidenefluoride) (PVDF) were mixed at a mass ratio of 75:20:5, and were dispersed in N-methylpyrrolidone (NMP). Then, the resulting mixture was coated onto a nickel foam substrate (1 × 1 cm) and dried in a vacuum

oven at 60 °C for 6 h. The loading mass of each electrode was about 2.7–3.2 mg. To investigate the electrochemical behavior of the as-prepared samples, cyclic voltammetry (CV) and galvanostatic charge/discharge experiments and electrochemical impedance spectroscopy (EIS) measurements were performed in a three-electrode mode using the as-prepared samples, platinum foil (1×1 cm), and an Ag/AgCl (KCl-saturated) electrode, as the working electrode, counter electrode, and reference electrode, respectively. Measurements were carried out in a 1 M Na_2SO_4 aqueous electrolyte at room temperature. CV and galvanostatic charge/discharge characteristics and EIS measurements were measured using a CHI 660C electrochemical workstation. EIS was recorded under the following conditions: AC voltage amplitude of 5 mV, frequency range of 10^5–0.1 Hz, and open circuit potential.

3. Results and discussion

The formation procedures of H-RGO/MnO_2 and S-RGO/MnO_2 composites are mainly composed of the following three steps: (i) synthesis of GO from graphite powder, (ii) formation of nanoneedle structure of MnO_2 particles onto GO surfaces and edges by the following reaction: $2KMnO_4 + 3MnCl_2 + 2H_2O \rightarrow 5MnO_2 + 2KCl + 4HCl$ [32], and (iii) chemical reduction of GO/MnO_2 using hydrazine hydrate and sodium borohydride.

Fig. 1 shows the XRD pattern of GO and GO/MnO_2, confirming the nanoneedle structure of MnO_2 before reduction of GO/MnO_2. The XRD pattern of GO reveals that the most intensive peak of GO (at around $2\theta = 11.5°$) corresponds to the (0 0 1) reflection, and the interlayer spacing is much larger than that of pristine graphite due to the introduction of oxygen-containing functional groups on the graphite sheets [34]. The diffraction peaks of the as-synthesized GO/MnO_2 are similar to those of the nanotetragonal phase of α–MnO_2 (JCPDS 44-0141, $a = 9.7845$ Å, $c = 2.8630$ Å), where the (0 0 1) reflection peak of layered GO has almost disappeared [30,32,35]. This indicates that homogeneous composites are formed with the surface of graphene oxide sheets covered by needle-like nanoscale MnO_2. This result correlates well with the previous studies that the diffraction peaks become weakened or even disappear whenever the regular stacks of GO are exfoliated [36].

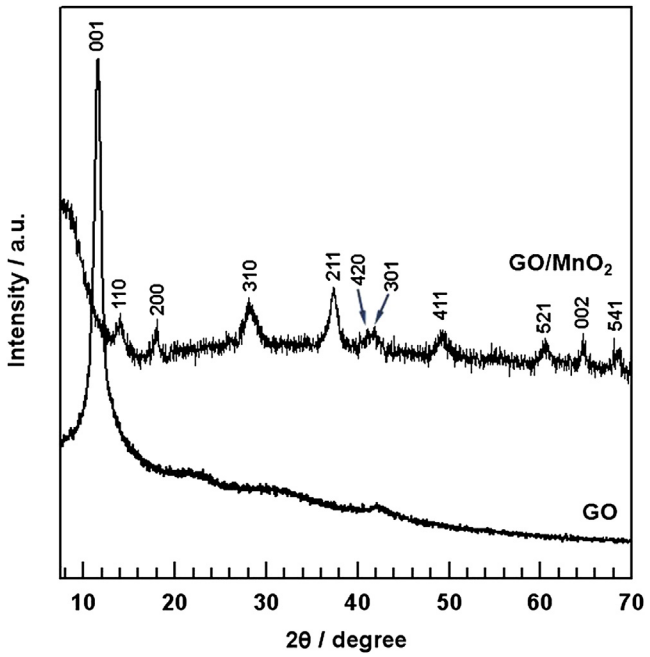

Fig. 1. XRD patterns of GO and GO/MnO_2.

FE-SEM images of GO, GO/MnO_2, H-RGO/MnO_2 and S-RGO/MnO_2 are shown in Fig. 2. Fig. 2(a) and (b) show GO and GO/MnO_2, respectively. In comparing Fig. 2(a) and (b), it can be clearly seen that GO sheets have been decorated homogeneously with the nanoneedle MnO_2 structures, and this is consistent with the XRD observations. Fig. 2(c) and (d) shows H-RGO/MnO_2 and S-RGO/MnO_2, respectively. After reduction of GO/MnO_2 to RGO/MnO_2 using hydrazine hydrate or sodium borohydride, there is no significant difference in the morphology between GO/MnO_2 and RGO/MnO_2. Interestingly, there are no obvious differences in the morphology of H-RGO/MnO_2 and S-RGO/MnO_2. Further, MnO_2 nanoneedles are well attached without obvious damage, indicating that both the hydrazine hydrate and sodium borohydride reducing agents effectively reduced the graphene oxide sheets.

To investigate the vibrational properties of the prepared samples, Raman spectroscopy was performed (Fig. 3). In the case of GO, the typical features in the Raman spectra are the G band at 1585 cm^{-1} and the D band at 1335 cm^{-1}. The G band is characteristic of sp^2-hybridized C–C bonds in a two-dimensional hexagonal lattice, and the D band corresponds to the defects and disordered carbon in the graphite layers [37,38]. As for the Raman spectrum of the GO/MnO_2, a new distinct sharp peak located at 640 cm^{-1} appeared, which can be attributed to the Mn–O vibrations perpendicular to the direction of the MnO_6 octahedral double chains of MnO_2 [39]. After being reduced by hydrazine hydrate and sodium borohydride, the peak belonging to the Mn–O vibrations is still observed at 640 cm^{-1} in the spectra of H-RGO/MnO_2 and S-RGO/MnO_2, respectively. The intensity ratio (I_D/I_G) of the D band to the G band of the GO/MnO_2 is about 0.97. However, after chemical reduction, it is observed that the I_D/I_G of H-RGO/MnO_2 and S-RGO/MnO_2 increased to 1.09 and 1.04, respectively. Moreover, H-RGO/MnO_2 shows a higher I_D/I_G ratio value than S-RGO/MnO_2, which corresponds to the use of hydrazine hydrate as a reducing agent. Hydrazine hydrate causes an increase in the number of defects by the removal of oxygen-containing functional groups [40]. Therefore, the successful integration of MnO_2 and chemically reduced graphene is occurred, and H-RGO/MnO_2 is more effectively reduced than S-RGO/MnO_2.

The compositions of as prepared GO/MnO_2, H-RGO/MnO_2 and S-RGO/MnO_2 composites are further investigated by TGA (Fig. 4). The experiments were performed up to 700 °C in air at a heating rate of 10 °C min^{-1}. Under these conditions, the GO and RGO sheets are burned up while MnO_2 turned into Mn_2O_3 [14]. Fig. 4 provides representative TGA curves of nanoneedle structures of MnO_2 (Mn), GO/MnO_2, H-RGO/MnO_2, S-RGO/MnO_2, GO and RGO. Typically, the weight loss values of Mn, GO/MnO_2, H-RGO/MnO_2, S-RGO/MnO_2, GO and RGO are found to be 12.5 wt.%, 26.4 wt.%, 28.91 wt.%, 28.93 wt.%, 92.1 wt.% and 100 wt.%, respectively. Accordingly, the mass ratio of MnO_2/(GO or RGO) for GO/MnO_2, H-RGO/MnO_2 and S-RGO/MnO_2 can be derived to be 4.7/1, 4.33/1 and 4.32/1, respectively. Therefore, the decrease in the mass ratios of H-RGO/MnO_2 and S-RGO/MnO_2 compared to GO/MnO_2 indicate that these reducing agents remove not only the functional groups on the graphene oxide sheets (i.e., hydroxyl, epoxy and carboxylic groups), but also the functional groups which are bonded to MnO_2. However, the decreased rate is marginal, and the mass ratio of H-RGO/MnO_2 and S-RGO/MnO_2 shows similar values. This means that H-RGO/MnO_2 and S-RGO/MnO_2 have a similar proportion of MnO_2 in the composites. Therefore, both hydrazine hydrate and sodium borohydride are effective reducing agents to preserve the nanoneedle structure of MnO_2 during reduction of GO to graphene.

Detailed surface information of GO and H-RGO/MnO_2 and S-RGO/MnO_2 was collected by X-ray photoelectron spectroscopy

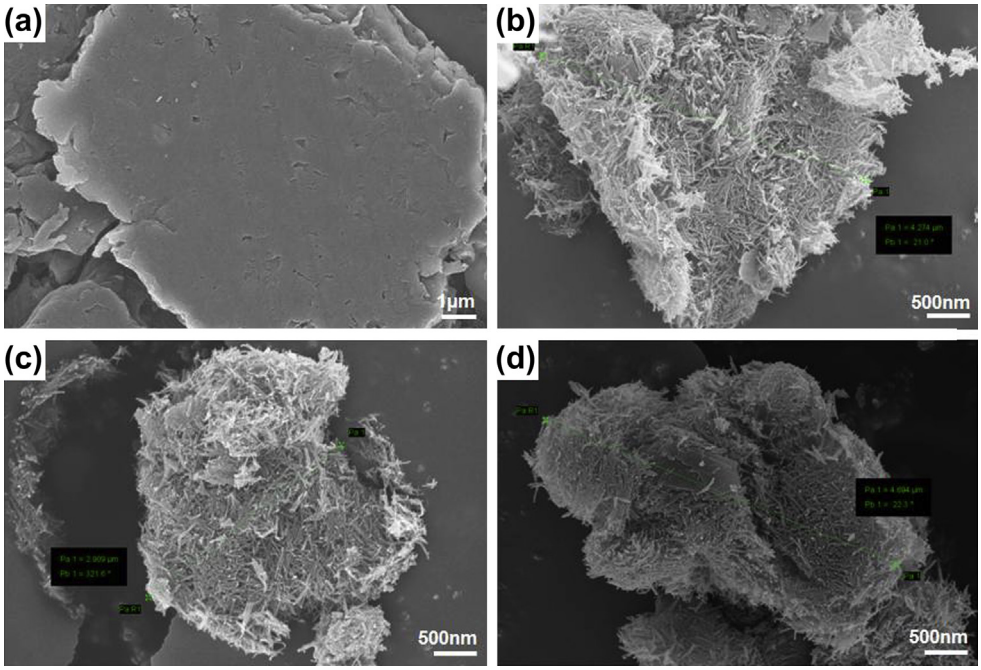

Fig. 2. FE-SEM images of GO, GO/MnO_2, H-RGO/MnO_2 and S-RGO/MnO_2. (a) GO; (b) GO/MnO_2; (c) H-RGO/MnO_2; (d) S-RGO/MnO_2.

(XPS), and the corresponding results are presented in Fig. 5. In the spectrum of GO, there are only two elements, namely, C and O. However, the Mn signal ($2p_{3/2}$, $2p_{1/2}$) emerges in the spectra of H-RGO/MnO_2 and S-RGO/MnO_2. This result implies that MnO_2 is successfully formed on the surface of chemically reduced graphene sheets. Fig. 5(b) and (c) shows the deconvoluted Mn 2p core-level spectra of H-RGO/MnO_2 and S-RGO/MnO_2, respectively. Fig. 5(b) and (c) shows the Mn 2p spectrum of H-RGO/MnO_2 and S-RGO/MnO_2 in which the peaks of Mn $2p_{3/2}$ and Mn $2p_{1/2}$ are located at 642.6 eV and 654.2 eV, respectively. Both H-RGO/MnO_2 and S-RGO/MnO_2 show the consistent spin-energy separation value is shown between the Mn $2p_{3/2}$ peak and the Mn $2p_{1/2}$ peak of 11.6 eV. These results are in accordance with previously reported data for Mn $2p_{3/2}$ and Mn $2p_{1/2}$ in nanoneedle structure of MnO_2 [35]. Fig. 5(d), (e) and (f) show the deconvoluted C 1s core-level spectra of GO/MnO_2, H-RGO/MnO_2 and S-RGO/MnO_2, respectively. Table 1 summarizes the differences of the GO/MnO_2, H-RGO/MnO_2 and S-RGO/MnO_2 in terms of their elemental composition and the resulting sheet resistance. The atomic ratio of carbon and oxygen is obtained by taking the ratio of the C 1s to O 1s peak areas in the XPS spectra. This ratio represents the degree of reduction, and it could be altered by the use of a different reducing agent. In order to

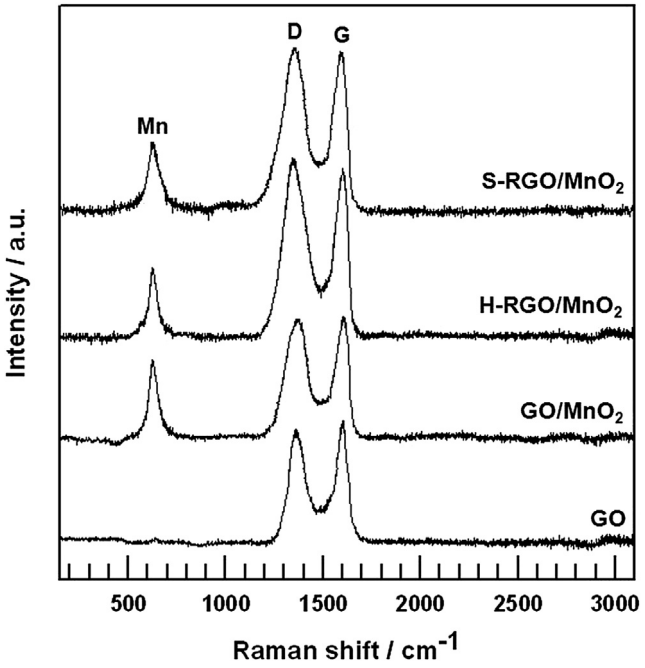

Fig. 3. Raman spectra of GO, GO/MnO_2, H-RGO/MnO_2 and S-RGO/MnO_2.

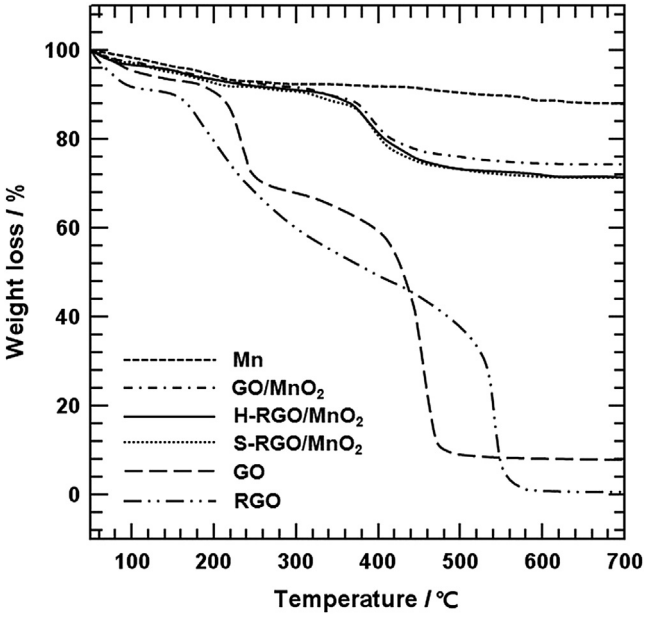

Fig. 4. TGA curves of Mn, GO, RGO, GO/MnO_2, H-RGO/MnO_2 and S-RGO/MnO_2.

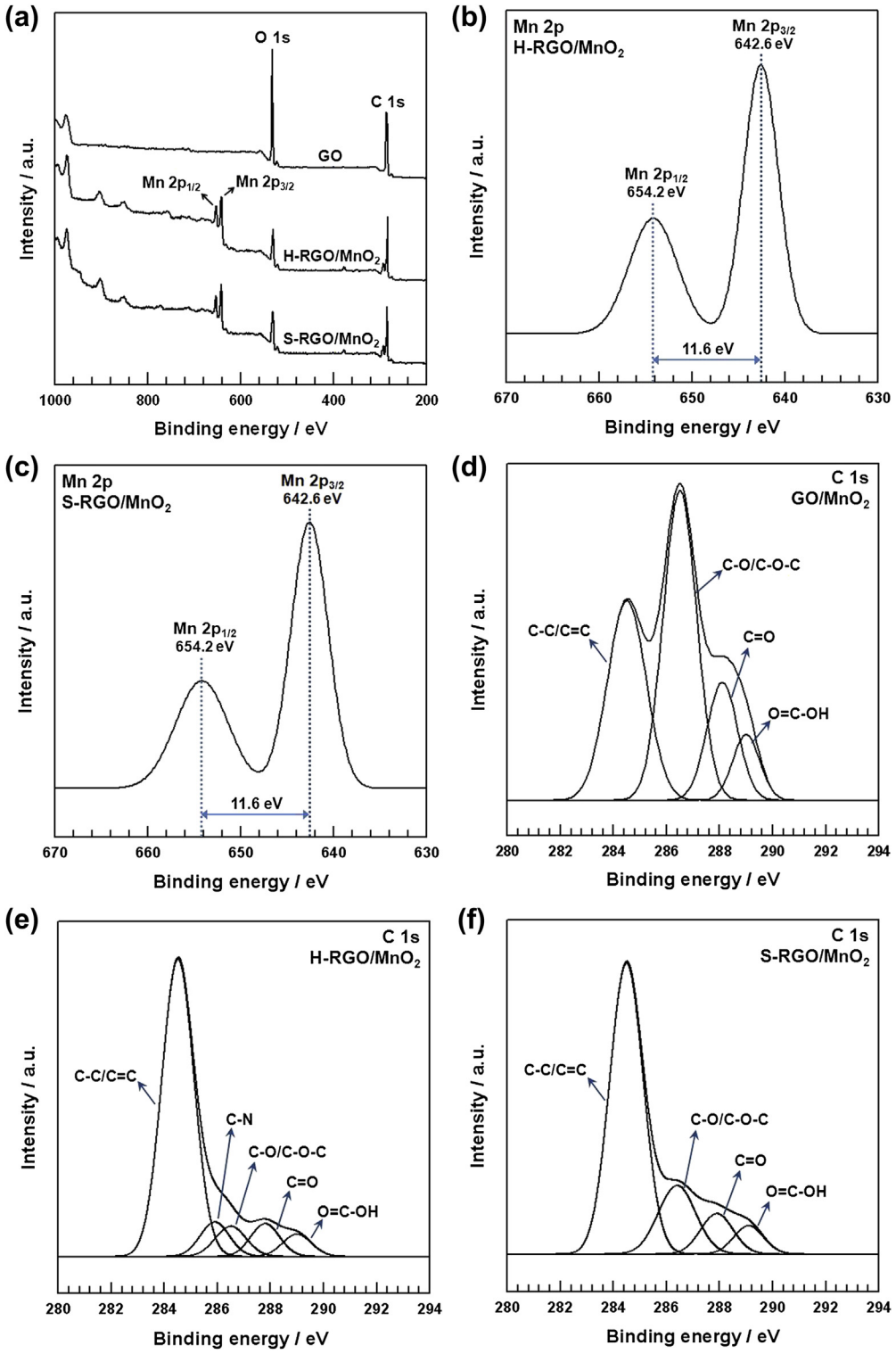

Fig. 5. XPS spectra of GO, H-RGO/MnO_2 and S-RGO/MnO_2. (a) Wide scan survey spectra; (b) XPS Mn 2p spectrum of H-RGO/MnO_2; (c) XPS Mn 2p spectrum of S-RGO/MnO_2; (d) XPS C 1s spectra of GO/MnO_2; (e) XPS C 1s spectra of H-RGO/MnO_2; (f) XPS C 1s spectra of S-RGO/MnO_2.

directly compare the effects of the reducing agent, the sheet resistance was measured for the pressed pellets of GO/MnO_2, H-RGO/MnO_2 and S-RGO/MnO_2 by the four-probe method. The GO/MnO_2 (Fig. 5(d)) shows strong binding energy peaks of aromatic C–C/C=C and–C–OH/C–O–C bonds at 284.5 and 286.5 eV, respectively, with several binding energy peaks of functional groups containing oxygen, such as C=O at 288.1 eV and O–C=O at 289.0 eV [41]. Compared with GO/MnO_2, the C 1s spectrum of H-RGO/MnO_2 (Fig. 5(e)) and S-RGO/MnO_2 (Fig. 5(f)) indicate that the area of the peak associated with C–C/C=C became predominant, while the area of C–O, C=O, and O=C–OH decreased dramatically. In H-RGO/MnO_2, which was reduced by hydrazine

Table 1
The C 1s peak position and the relative atomic percentages of various functional groups in GO/MnO_2, H-RGO/MnO_2 and S-RGO/MnO_2 and their sheet resistances.

	C:O ratio	Fitting of the C 1s peak binding energy [eV] (relative atomic percentage [%])					Sheet resistance [kΩ sq^{-1}]
		C–C/C=C	C–N	C–O/C–O–C	C=O	O=C–OH	
GO/MnO_2	2.6	284.5 (32.9)	–	286.5 (44.1)	288.1 (15.4)	289 (7.6)	8914
H-RGO/MnO_2	4.7	284.5 (72.8)	285.9 (7.6)	286.5 (7.2)	287.8 (7.5)	289 (4.9)	432
S-RGO/MnO_2	4.3	284.5 (67.2)	–	286.4 (17.8)	287.9 (9.1)	289.1 (5.9)	791

hydrate, the appearance of a peak indicating a C–N bond is assigned because the carbonyl and carboxylate groups finally formed C=N bonds associated with hydrazones [42]. The heterocarbon component of the H-RGO/MnO_2 (27.2 at.%) and S-RGO/MnO_2 (32.8 at.%) markedly decrease beyond that of GO/MnO_2 (66.3 at.%). H-RGO/MnO_2 also exhibits a much lower heterocarbon component than that of S-RGO/MnO_2, which indicated that hydrazine reduction is more effective at increasing the hydrocarbon component since hydrazine reduction is known to form hydrocarbons from carbonyl groups [40,42,43], whereas sodium borohydride reduction forms residual hydroxyl functional groups [44]. Electrical conductivity is known to be directly related to oxygen content. Therefore, the use of hydrazine hydrate as the reducing agent is more beneficial than sodium borohydride in lowering the sheet resistance due to the fact that it yields the lowest concentration of heterocarbon. Therefore, although both hydrazine hydrate and sodium borohydride cause a reducing effect, hydrazine hydrate is a better reducing agent than sodium borohydride for GO/MnO_2.

To explore the potential applications for supercapacitors, the samples were fabricated into supercapacitor electrodes and were characterized with cyclic voltammograms and galvanostatic charge/discharge measurements. Fig. 6(a) shows the CV curves of H-RGO/MnO_2, S-RGO/MnO_2, and GO/MnO_2 at a scan rate of 10 mV s^{-1} in 1 M Na_2SO_4 electrolyte. CV curves for H-RGO/MnO_2 and S-RGO/MnO_2 and GO/MnO_2 electrodes are almost ideally rectangular in shape, without obvious redox peaks, indicating that the composites have ideal capacitive behavior [28]. Clearly, the H-RGO/MnO_2 and S-RGO/MnO_2 electrodes show a much larger integrated area than the GO/MnO_2 electrode, which indicates excellent electrochemical performance. The excellent electrochemical performance of H-RGO/MnO_2 and S-RGO/MnO_2 composites may be attributed to the excellent electric conductive properties of graphene. The graphene oxide cannot form electronic conductive channels due to its low electrical conductivity. As illustrated in Fig. 3, the intensity ratio (I_D/I_G) of the D band to the G band of the GO/MnO_2 was about 0.97. However, after the hydrazine and sodium borohydride reduction process, the I_D/I_G ratio of H-RGO/MnO_2 and S-RGO/MnO_2 increased to 1.09 and 1.04, respectively, in contrast to the GO/MnO_2. As shown in Table 1, the H-RGO/MnO_2 and S-RGO/MnO_2 exhibited much lower sheet resistance value compared to GO/MnO_2. This implies that GO/MnO_2 was effectively reduced to RGO/MnO_2 using hydrazine hydrate and sodium borohydride as a reducing agent. Also, as illustrated in Fig. 2, the nanoneedle-structure MnO_2 fully formed on the graphene surface can help increase the specific area, which can form pores for ion-buffering reservoirs to improve the diffusion rate of Na^+ ions and good alignment of nanoneedles that can provide well-ordered tunnels, convenient for the insertion/extraction of Na^+ cations into/from MnO_2 [32]. Nanoscale MnO_2 particles can greatly reduce the diffusion length over which Na^+ must transfer during the charge/discharge process, improving the electrochemical utilization of MnO_2. Therefore, reduced graphene oxide in H-RGO/MnO_2 and S-RGO/MnO_2 acts not only as a support for formation of nanoneedle structure of MnO_2, but also provides electrically conductive channels. Furthermore, there are obvious differences between the H-RGO/MnO_2 and S-RGO/MnO_2 electrodes. The H-RGO/MnO_2 electrode shows a larger integrated area than that of the S-RGO/MnO_2. The excellent electrochemical performance of H-RGO/MnO_2 electrode may be attributed to their electrical conductivity [45]. As indicated in Table 1, it can be assumed that the H-RGO/MnO_2 composite has a much lower sheet resistance value than that of S-RGO/MnO_2. This is due to the increased oxygen-containing functional groups (e.g., C–O, C–O–C, C=O and O=C–OH) of the S-RGO/

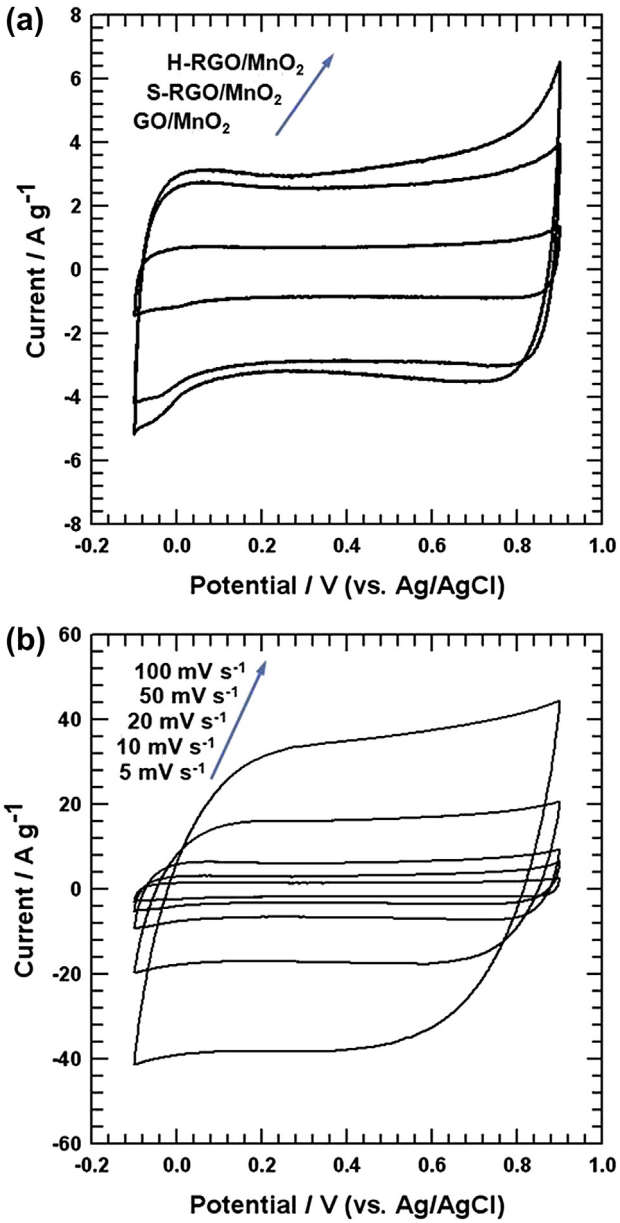

Fig. 6. (a) CV curves of GO/MnO_2, H-RGO/MnO_2 and S-RGO/MnO_2 electrodes at 10 mV s^{-1}; (b) CV curves of H-RGO/MnO_2 electrode at different scan rates of 5, 10, 20, 50 and 100 mV s^{-1}.

MnO_2 which decrease the electric conductivity. Moreover, this is also correlated to the I_D/I_G ratio of H-RGO/MnO_2 and S-RGO/MnO_2 in the Raman spectra. It is observed that the I_D/I_G ratio of the H-RGO/MnO_2 shows a slightly higher value than that of S-RGO/MnO_2, which corresponds to the increased effectiveness of hydrazine hydrate in removing oxygen-containing functional groups over sodium borohydride. Therefore, these results reveal that the reducing effect of hydrazine hydrate is more effective than sodium borohydride in the reduction of GO/MnO_2, which was further confirmed through the EIS study. To obtain more information on the capacitive performance of the prepared composite, H-RGO/MnO_2 electrode was subjected to detailed measurements. Fig. 6(b) displays the CV curves of H-RGO/MnO_2 electrode at different scan rates of 5, 10, 20, 50, and 100 mV s^{-1} in 1 M Na_2SO_4 electrolyte. In the case of H-RGO/MnO_2, the CV profiles still retain a relatively rectangular shape with high symmetry, without an obvious distortion with the increasing potential scan rates. This indicates the ideal capacitive properties and excellent reversibility of H-RGO/MnO_2 electrode.

Impedance measurements were performed for GO/MnO_2, H-RGO/MnO_2 and S-RGO/MnO_2 electrodes using the EIS as shown in Fig. 7. The EIS data are analyzed using Nyquist plots. The Nyquist plots consist of three parts: (i) a semicircle in the high-to-medium frequencies region indicating the intersection point at the Z' axis representing the contact resistance and the diameter of which represents the charge transport resistance (R_{ct}); (ii) a straight line with a slope of 45° in the low-frequency range, which corresponds to semi-infinite Warburg impedance resulting from the frequency dependence of ion diffusion/transport in the electrolyte; and (iii) a vertical line at the very low frequencies, which is due to the accumulation of ions at the bottom of the pores of the electrode. The nearly vertical line demonstrates a good capacitive behavior without diffusion limitation. In comparison of the impedance plots of GO/MnO_2, H-RGO/MnO_2 and S-RGO/MnO_2 electrodes, it is obvious that the electrodes listed in order of the diameter of the semicircle are GO/MnO_2 > S-RGO/MnO_2 > H-RGO/MnO_2. Table 2 summarizes the R_{ct} values of the GO/MnO_2, H-RGO/MnO_2 and S-RGO/MnO_2 electrodes. This can be explained by the sheet resistance behaviors of GO/MnO_2, H-RGO/MnO_2 and S-RGO/MnO_2 electrodes. As indicated in Table 1, the sheet resistances of GO/MnO_2, H-RGO/MnO_2 and S-RGO/MnO_2 composites are 8914, 432 and 791 kΩ sq^{-1}, respectively. Therefore, the diameter of the semicircles gradually decreased with increasing oxygen-containing functional groups, an indication of decreasing trend of charge transfer resistance, in line with the linear reduction in sheet resistance. Furthermore, the straight lines at the very low frequencies of both H-RGO/MnO_2 and S-RGO/MnO_2 show a nearly vertical shape, indicating rapid ion diffusion in the electrolyte and adsorption onto the electrode surface [35,48,49].

Table 2
Charge transfer resistance values of GO/MnO_2, H-RGO/MnO_2 and S-RGO/MnO_2.

	GO/MnO_2	H-RGO/MnO_2	S-RGO/MnO_2
R_{ct} (Ω)	1.32	0.63	0.97

The galvanostatic charge/discharge measurements of GO/MnO_2, H-RGO/MnO_2 and S-RGO/MnO_2 electrodes were carried out in 1 M Na_2SO_4 between −0.1 and 0.9 V at current densities of 10 mA cm^{-2}. As illustrated in Fig. 8, during the charging and discharging steps, the charge curves of H-RGO/MnO_2 and S-RGO/MnO_2 electrodes are almost symmetric to their corresponding discharge counterparts, with slight curvature, indicating pseudocapacitive and double layer contributions [46]. However, in comparing the discharging curves of H-RGO/MnO_2 and S-RGO/MnO_2 electrodes, the H-RGO/MnO_2 electrode exhibits much longer discharging time, which is consistent with specific capacitance behavior since discharging time is directly proportional to the specific capacitance of electrodes.

The specific capacitances (C_s) are calculated from the CV curves according to the following equation [47]:

$$C_s = \frac{1}{v(V_c - V_a)} \int_{V_a}^{V_c} I(V)\mathrm{d}V \quad (1)$$

where C_s is the specific capacitance (F g^{-1}), v is the potential scan rate (mV s^{-1}), $V_c - V_a$ represents the sweep potential range (V) and $I(V)$ denotes the response current density (A g^{-1}). Fig. 9 presents

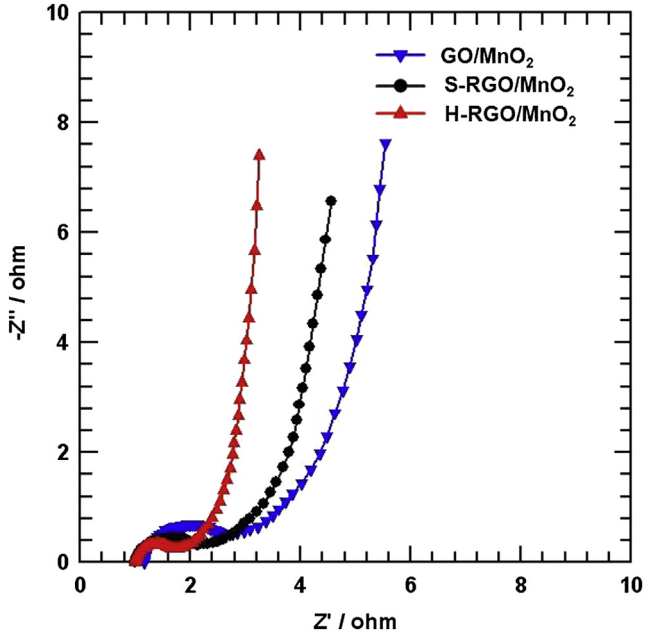

Fig. 7. Nyquist plots of GO/MnO_2, H-RGO/MnO_2 and S-RGO/MnO_2 electrodes.

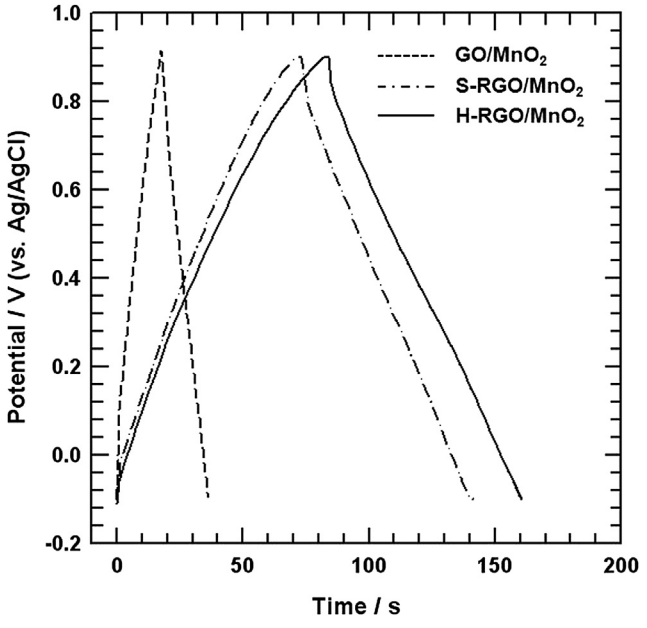

Fig. 8. Galvanostatic charge/discharge curves of GO/MnO_2, H-RGO/MnO_2 and S-RGO/MnO_2 electrodes at current density of 10 mA cm^{-2}.

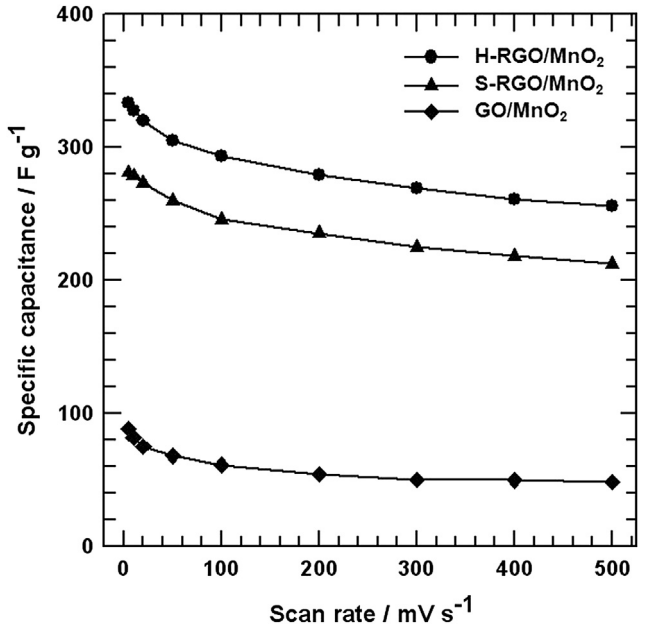

Fig. 9. Specific capacitance of GO/MnO_2, H-RGO/MnO_2 and S-RGO/MnO_2 electrodes at different scan rates of 5, 10, 20, 50, 100, 200, 300, 400 and 500 mV s^{-1}.

the relationship between the C_s and the scan rate of the GO/MnO_2, H-RGO/MnO_2 and S-RGO/MnO_2 electrodes. The calculated C_s values of GO/MnO_2, H-RGO/MnO_2 and S-RGO/MnO_2 electrodes at 10 mV s^{-1} are 81.5, 327.5 and 278.6 F g^{-1}, respectively. In comparison with GO/MnO_2, the improved electrochemical performance of H-RGO/MnO_2 and S-RGO/MnO_2 electrodes is attributed to the intrinsic electrical double layer capacitance of graphene.

Cycle stability behavior is very important for supercapacitors. The cycling stability of the GO/MnO_2, H-RGO/MnO_2 and S-RGO/MnO_2 electrodes was also evaluated by CV test at a scan rate of 10 mV s^{-1} for 1000 cycles. As shown in Fig. 10, the specific capacitances of GO/MnO_2, H-RGO/MnO_2 and S-RGO/MnO_2 decrease

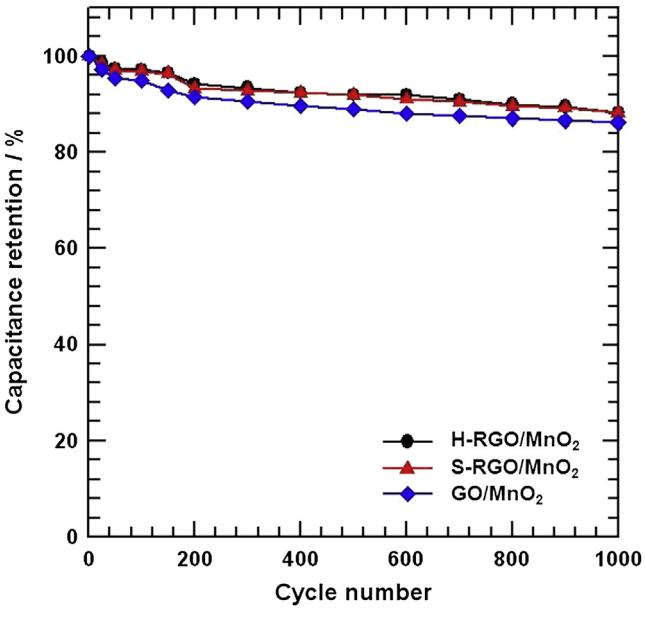

Fig. 10. Cycling stability of the GO/MnO_2, H-RGO/MnO_2 and S-RGO/MnO_2 electrodes measured at 10 mV s^{-1}.

gradually in the initial 400 cycles. After 1000 cycles, the capacitance retentions for GO/MnO_2, H-RGO/MnO_2 and S-RGO/MnO_2 are 86.12%, 88.26% and 88.19%, respectively, demonstrating that the cycle stabilities of H-RGO/MnO_2 and S-RGO/MnO_2 are similar. The capacitance of the GO/MnO_2, H-RGO/MnO_2 and S-RGO/MnO_2 electrodes after 1000 cycles is also smaller than that of the first cycle, which may be ascribed to the loss of the active materials in the electrode and/or the mass loss of the electrode after 1000 cycles [29].

4. Conclusions

Graphene/MnO_2 composites are synthesized by a chemical reduction of GO/MnO_2 using reducing agents, and their structural characteristics and electro-chemical properties are evaluated for potential applications in supercapacitors. In this procedure, an isopropyl alcohol–water solution is employed as the reacting system, which is beneficial for the oriented growth of the crystal species to form MnO_2 on the graphene oxide sheets. Hydrazine hydrate and sodium borohydride are used as the reducing agents. The H-RGO/MnO_2 and S-RGO/MnO_2 are obtained by chemical reduction of GO/MnO_2 using hydrazine hydrate and sodium borohydride reducing agents, respectively. The nanoneedle structure of MnO_2 increases the specific area. Further, reduced graphene oxide acts as not only as a support for the deposition of MnO_2 particles, but also provides electrically conductive channels. Therefore, graphene/MnO_2 composites are beneficial to increase both the electrical conductivity and the accessible surface area, resulting in excellent electrochemical performance. The specific capacitance of H-RGO/MnO_2 and S-RGO/MnO_2 electrodes at scan rate of 10 mV s^{-1} is 327.5 and 278.6 F g^{-1}, respectively. After 1000 cycles, the capacitances of H-RGO/MnO_2 and S-RGO/MnO_2 electrodes decrease by 11.74% and 11.81% from the initial capacitance, respectively, indicating excellent electrochemical stability. The differences in specific capacitance are explained by the electrical conductivities of the H-RGO/MnO_2 and S-RGO/MnO_2 electrodes. Therefore, the lower content of oxygen atoms can contribute to an improvement in electrical conductivity and can lead to the formation of more effective electronic conductive channels. Therefore, both hydrazine hydrate and sodium borohydride are effective reducing agents that improve electrochemical properties, but hydrazine hydrate is more effective when reducing GO/MnO_2. These results illustrate that this procedure is a promising method for the synthesis of electrode materials for supercapacitors.

Acknowledgements

This research was supported by Basic Science Research Program through the National Research Foundation of Korea (NRF) funded by the Ministry of Education, Science and Technology (2012R1A1A2008884).

References

[1] V. Subramanian, H. Zhu, R. Vajtai, P.M. Ajayan, B. Wei, J. Phys. Chem. B. 109 (2005) 20207–20214.
[2] A.L. Mohana, R.F. Estaline, A. Imran, J.S. Ramaprabhu, Nanoscale Res. Lett. 3 (2008) 145–151.
[3] A.C.-G. Karina, L.-C. Monica, C.-P. Nieves, G.-R. Pedro, Adv. Funct. Mater. 15 (2005) 1125–1133.
[4] R. Kotz, M. Carlen, Electrochim. Acta 45 (2000) 2483–2496.
[5] Z. Chen, Y. Qin, D. Weng, Q. Xiao, Y. Peng, X. Wang, H. Li, F. Wei, Y. Lu, Adv. Funct. Mater. 19 (2009) 3420–3426.
[6] P. Simon, Y. Gogotsi, Nat. Mater. 7 (2008) 845–854.
[7] S.-L. Chou, J.-Z. Wang, S.-Y. Chew, H.-K. Liu, S.-X. Dou, Electrochem. Commun. 10 (2008) 1724–1727.
[8] S.B. Ma, K.W. Nam, W.S. Yoon, X.Q. Yang, K.Y. Ahn, K.H. Oh, K.B. Kim, J. Power Sources 178 (2008) 483–489.

[9] S. Komaba, A. Ogata, T. Tsuchikawa, Electrochem. Commun. 10 (2008) 1435–1437.
[10] S.B. Ma, K.Y. Ahn, E.S. Lee, K.H. Oh, K.B. Kim, Carbon 45 (2007) 375–382.
[11] N. Nagarajan, M. Cheong, I. Zhitomirsky, Mater. Chem. Phys. 103 (2007) 47–53.
[12] A.E. Fischer, K.A. Pettigrew, D.R. Rolison, R.M. Stroud, J.W. Long, Nano Lett. 7 (2007) 281–286.
[13] X. Dong, W. Shen, J. Gu, L. Xiong, Y. Zhu, H. Li, J. Shi, J. Phys. Chem. B 110 (2006) 6015–6019.
[14] M.N. Patel, X. Wang, B. Wilson, D.A. Ferrer, S. Dai, K.J. Stevenson, K.P. Johnston, J. Mater. Chem. 20 (2010) 390–398.
[15] Y. Hou, Y. Cheng, T. Hobson, J. Liu, Nano Lett. 10 (2010) 2727–2733.
[16] E. Raymundo-Pinero, V. Khomenko, E. Frackowiak, F. Beguin, J. Electrochem. Soc. 152 (2005) A229–A235.
[17] K.R. Prasad, N. Miura, J. Power Sources 135 (2004) 354–360.
[18] X. Jin, W. Zhou, S. Zhang, G.Z. Chen, Small 3 (2007) 1513–1517.
[19] K.S. Novoselov, A.K. Geim, S.V. Morozov, D. Jiang, Y. Zhang, S.V. Dubonos, I.V. Grigorieva, A.A. Firsov, Science 306 (2004) 666–669.
[20] S.-Y. Yang, K.-H. Chang, H.-W. Tien, Y.-F. Lee, S.-M. Li, Y.-S. Wang, J.-Y. Wang, C.-C.M. Ma, C.-C. Hu, J. Mater. Chem. 21 (2011) 2374–2380.
[21] H. Wang, H.S. Casalongue, Y. Liang, H. Dai, J. Am. Chem. Soc. 132 (2010) 7472–7477.
[22] L. Qiu, X. Yang, X. Gou, W. Yang, Z.-F. Ma, G.G. Wallace, D. Li, Chem. Eur. J. 16 (2010) 10653–10658.
[23] Z. Fan, J. Yan, L. Zhi, Q. Zhang, T. Wei, J. Feng, M. Zhang, W. Qian, F. Wei, Adv. Mater. 22 (2010) 3723–3728.
[24] S. Park, R.S. Ruoff, Nat. Nanotechnol. 4 (2009) 217–224.
[25] S. Biswas, L.T. Drzal, Chem. Mater. 22 (2010) 5667–5671.
[26] Z.-S. Wu, D.-W. Wang, W. Ren, J. Zhao, G. Zhou, F. Li, H.-M. Cheng, Adv. Funct. Mater. 20 (2010) 3595–3602.
[27] Y. Xu, K. Sheng, C. Li, G. Shi, ACS Nano 4 (2010) 4324–4330.
[28] J. Yan, Z. Fan, T. Wei, W. Qian, M. Zhang, F. Wei, Carbon 48 (2010) 3825–3833.
[29] Z. Li, J. Wang, S. Liu, X. Liu, S. Yang, J. Power Sources 196 (2011) 8160–8165.
[30] S. Chen, J. Zhu, Q. Han, Z. Zheng, Y. Yang, X. Wang, Cryst. Growth Des. 9 (2009) 4356–4361.
[31] S. Devaraj, N. Munichandraiah, J. Phys. Chem. C 112 (2008) 4406–4417.
[32] S. Chen, J. Zhu, X. Wu, Q. Han, X. Wang, ACS Nano 4 (2010) 2822–2830.
[33] H.J. Shin, K.K. Kim, B. Anass, S.M. Yoon, H.K. Park, I.S. Jung, M.H. Jin, H.K. Jeong, J.M. Kim, J.Y. Choi, Y.H. Lee, Adv. Funct. Mater. 19 (2009) 1987–1992.
[34] C. Xu, X. Wu, J. Zhu, X. Wang, Carbon 46 (2008) 386–389.
[35] L. Mao, K. Zhang, H. Chan, J. Wu, J. Mater. Chem. 22 (2012) 1845–1851.
[36] C. Xu, X. Wang, J. Zhu, J. Phys. Chem. C 112 (2008) 19841–19845.
[37] A.C. Ferrari, J. Robertson, Philos. Trans. R. Soc. Lond. A 362 (2004) 2477–2512.
[38] L.G. Cancado, M.A. Pimenta, B.R.A. Neves, M.S.S. Dantas, A. Jorio, Phys. Rev. Lett. 93 (2004) 247401.
[39] T. Gao, M. Glerup, F. Krumeich, R. Nesper, H. Fjellvag, P. Norby, J. Phys. Chem. C 112 (2008) 13134–13140.
[40] Sasha Stankovich, Dmitriy A. Dikin, Richard D. Piner, Kevin A. Kohlhaas, Alfred Kleinhannes, Yuanyuan Jia, Yue Wu, SonBinh T. Nguyen, Rodney S. Ruoff, Carbon 45 (2007) 1558–1565.
[41] H.G. Im, J.H. Kim, Carbon 50 (2012) 5429–5440.
[42] P.G. Ren, D.X. Yan, X. Ji, T. Chen, Z.M. Li, Nanotechnology 22 (2011) 055705.
[43] N. Kishner, J. Russ. Phys. Chem. Soc. 43 (1911) 582–595.
[44] Y.-Q. Cao, Z. Dai, B.-H. Chen, R. Liu, J. Chem. Technol. Biotechnol. 80 (2005) 834–836.
[45] S.R. Sivakkumar, J.M. Ko, D.Y. Kim, B.C. Kim, G.G. Wallace, Electrochim. Acta 52 (2007) 7377–7385.
[46] Z. Li, Y. Mi, Z. Liu, S. Liu, S. Yang, J. Wang, J. Mater. Chem. 21 (2011) 14706–14711.
[47] X. Xie, L. Gao, Carbon 45 (2007) 2365–2373.
[48] Tarik Bordjiba, Daniel Belanger, J. Electrochem. Soc. 156 (2009) A378–A384.
[49] Zhen-Dong Huang, Biao Zhang, Rui Liang, Qing-Bin Zheng, Sei Woon Oh, Xiu-Yi Lin, Nariman Yousefi, Jang-Kyo Kim, Carbon 50 (2012) 4239–4251.